

2018

# Surface currents from hourly variations of suspended particulate matter from Geostationary Ocean Color Imager data

Kyung-Ae Park

Min-Sun Lee

*See next page for additional authors*

Creative Commons License



This work is licensed under a [Creative Commons Attribution-Noncommercial-No Derivative Works 4.0 License](https://creativecommons.org/licenses/by-nc-nd/4.0/).

Follow this and additional works at: <https://digitalcommons.uri.edu/gsofacpubs>

---

---

**Authors**

Kyung-Ae Park, Min-Sun Lee, Ji-Eun Park, David Ullman, Peter C. Cornillon, and Young-Je Park

---



## Surface currents from hourly variations of suspended particulate matter from Geostationary Ocean Color Imager data

Kyung-Ae Park, Min-Sun Lee, Ji-Eun Park, David Ullman, Peter C. Cornillon & Young-Je Park

To cite this article: Kyung-Ae Park, Min-Sun Lee, Ji-Eun Park, David Ullman, Peter C. Cornillon & Young-Je Park (2018) Surface currents from hourly variations of suspended particulate matter from Geostationary Ocean Color Imager data, International Journal of Remote Sensing, 39:6, 1929-1949, DOI: [10.1080/01431161.2017.1416699](https://doi.org/10.1080/01431161.2017.1416699)

To link to this article: <https://doi.org/10.1080/01431161.2017.1416699>



© 2018 The Author(s). Published by Informa UK Limited, trading as Taylor & Francis Group.



Published online: 03 Jan 2018.



Submit your article to this journal [↗](#)



Article views: 341



View Crossmark data [↗](#)



Citing articles: 1 View citing articles [↗](#)

# Surface currents from hourly variations of suspended particulate matter from Geostationary Ocean Color Imager data

Kyung-Ae Park<sup>a</sup>, Min-Sun Lee<sup>b</sup>, Ji-Eun Park<sup>b</sup>, David Ullman<sup>c</sup>, Peter C. Cornillon<sup>c</sup> and Young-Je Park<sup>d</sup>

<sup>a</sup>Department of Earth Science Education, Seoul National University, Seoul, Korea; <sup>b</sup>Department of Science Education, Seoul National University, Seoul, Korea; <sup>c</sup>Graduate School of Oceanography, University of Rhode Island, Kingston, RI, USA; <sup>d</sup>Korea Ocean Satellite Center, Korea Institute of Ocean Science and Technology, Ansan, Korea

## ABSTRACT



Surface currents in Korean coastal regions were obtained using the maximum cross-correlation method applied to hourly suspended particulate matter images from the Geostationary Ocean Color Imager. Preliminary current vectors were filtered out by applying a series of quality-control procedures. The current vectors resulting from the tests were compared with the currents from a numerical model with tide and wind field. It was found that the estimated currents were more similarly to the currents caused by both tide and wind. A high degree of discrepancy was detected in regions of strong tidal currents, where the fundamental assumption of horizontal movement was limited due to the dominant vertical tidal mixing in the shallow region. The hourly rotations of the current vectors within a day were clarified by a comparison of the time-varying orientation angles of tidal ellipses. This study emphasized how to understand the short-term surface flows from hourly high-resolution geostationary satellite images.

## ARTICLE HISTORY

Received 6 August 2017  
Accepted 29 November 2017

## 1. Introduction

A great deal of effort has long been expended in the past to derive surface currents from successive pairs of satellite-derived sea surface temperature (SST) images using a maximum cross-correlation method (MCC) or an inverse method with regard to a temperature conservation equation (e.g. Leese, Novak, and Clark 1971; Ninnis, Emery, and Collins 1986; Emery et al. 1986; Kelly 1989; Tokmakian, Strub, and McClean-Padman 1990; Bowen et al. 2002; Zavialov et al. 2002). Matthews and Emery (2009) estimated currents off the California coast from brightness temperature images instead of SST images to avoid problems associated with noise amplification caused by the SST algorithm. More recently, multi-satellite variables from optical remote-sensing data, such as chlorophyll-*a* concentration data or suspended particulate matter (SPM) data, have been utilized to

**CONTACT** Kyung-Ae Park  [kapark@snu.ac.kr](mailto:kapark@snu.ac.kr)  Department of Earth Science Education, Seoul National University, Seoul 08826, Korea

© 2018 The Author(s). Published by Informa UK Limited, trading as Taylor & Francis Group.  
This is an Open Access article distributed under the terms of the Creative Commons Attribution-NonCommercial-NoDerivatives License (<http://creativecommons.org/licenses/by-nc-nd/4.0/>), which permits non-commercial re-use, distribution, and reproduction in any medium, provided the original work is properly cited, and is not altered, transformed, or built upon in any way.

determine oceanic currents using these methods. Combining current retrievals from Advanced Very High-Resolution Radiometer thermal data and Sea-viewing Wide Field-of-view Sensor ocean colour imagery has been shown to provide improved spatial coverage (Crocker et al. 2007).

The launch of the first geostationary satellite for ocean colour (GOCI, the Geostationary Ocean Color Imager) and the hourly imagery produced from this data stream has recently provided the capability for obtaining surface currents on timescales (hours) that were unattainable with prior polar orbiter observations. Studies of oceanic currents using high temporal resolution GOCI variables have been performed using either the normalized MCC approach or the cosine similarity method (Choi et al. 2013; Yang et al. 2014), the latter of which is fundamentally identical to the MCC method but excluding the removal of the mean value.

The MCC method itself is robust to an ideal field; however, serious problems and significant limitations arise when applied to actual satellite data. The MCC method is known to be deficient when used to detect surface current vectors around a meso-scale eddy in which the current is predominantly along isotherms. Many attempts to overcome this type of limitation, related to rotation and deformation, have been conducted by adopting a rotating coordinate system around the eddy with the MCC method (Kamachi 1989). This study addresses some of the problems which arise when obtaining ocean surface velocities from a pair of sequential GOCI images over a short period of time.

GOCI has been used to observe wide sea areas around Korea since June 2010. The Yellow Sea is characterized by high turbid water, especially along the south-western coast of Korea, as shown in Figure 1. This turbid water is well known to be induced by strong tidal currents at the coastal region due to its shallow bathymetry (Lee et al. 1987; Lee and Chough 1989). A significant amount of land-derived materials flows into the shelf from rivers in the East Asian region and is dispersed in the form of SPM by the strong tidal currents. Such SPM distributions from satellite ocean colour images are readily detected along the western coastal regions of Korea.

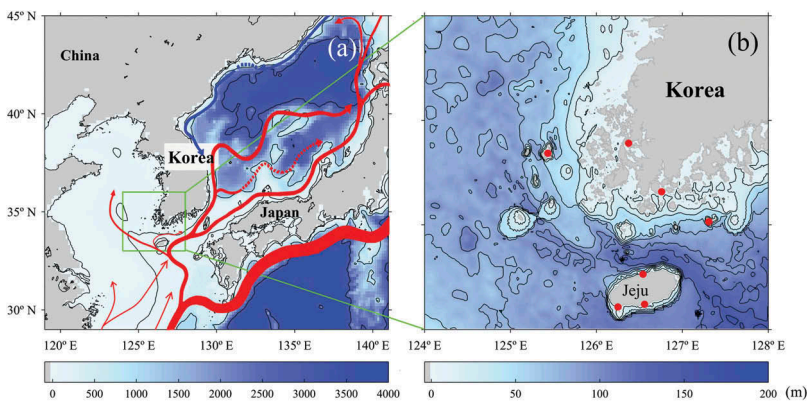


**Figure 1.** (a) Currents around Korea and (b) study area, where the blue colours represent the water depths, the red dots are the locations of the tidal gauge stations.

SPM (or total suspended matter) has been recognized as an important oceanic variable due to its significant role in our understanding of the spatial and temporal variation of currents, circulation, water clarity, contaminants, and nutrients (Martin and Meybeck 1979; Findlay, Pace, and Lints 1991; D'Sa, Miller, and McKee 2007). Tracing changes in the spatial distribution of SPM makes it possible to identify water flows and the transport of organic carbon (Yiğiterhan, Murray, and Tuğrul 2011). In the study region, the SPM concentration has played an important role in our understanding of oceanic currents, including tidal currents and other physical–biological processes.

The study region in [Figure 1\(b\)](#) exhibits seasonally dependent weak coastal currents along the coastal boundary and the westward flowing Jeju warm current through the Jeju Strait. The coastline and bathymetry are spatially complex such that the currents, which are dominated by tides (Moon, Hirose, and Yoon 2009), tend to be highly spatially variable as well. Satellite-derived SPM imagery at the high spatial resolution provided by GOCI is thus valuable if these data can be used to reliably estimate surface currents and their spatial variability in the region. A key issue with respect to the estimation of currents using the MCC method is the methodology with which to screen out noisy current vectors. The objectives of this study are (1) to estimate surface currents from GOCI SPM data using the MCC method, (2) to develop and test a quality-control procedure to eliminate unreliable current vectors, (3) to compare the retrieved current vectors with tide and wind-induced currents from a numerical model, (4) to derive tidal ellipses and angular velocities from short-term satellite images, and (5) to present the characteristics and potential causes of the differences between the derived and the simulated current vectors.

## 2. Data and methods

### 2.1. Deriving surface currents from satellite SPM images

GOCI measurements offer the unprecedented advantage of oceanic optical observations with a temporal repetition period of one hour. This technology has brought new opportunities to those who investigate and quantify short-term variations at high spatial resolutions (about 500 m), as doing so has long been impossible with numerous near-polar orbiting satellites and many other types of geostationary satellites. GOCI can be used to measure radiance levels in the visible band and these can be used to estimate SPM concentrations and other optical oceanic variables at hourly intervals.

Clear-sky images without any clouds over the entire region for a day are rarely obtainable due to the frequent movement of clouds as well as the formation of fog due to the abrupt changes in atmospheric and oceanic conditions in this region (Cho, Kim, and Kim 2000). There have been a small number of GOCI image pairs which cover the entire region. As one example of sufficient coverage for the derivation of surface currents, we selected GOCI SPM images for 8 hours from 9 a.m. to 4 p.m. on 28 April 2012. [Figure 2](#) shows these hourly SPM images for the coastal region southwest of Korea and Jeju Island in the Yellow Sea, which is the area of interest for the purposes of this study. During the first 5 hours, clouds were relatively sparse and limited to the southern portion of the image around 34° N. However, from 2 p.m. to 4 p.m., clouds (as denoted by the white pixels in [Figure 2](#)) began to preclude the estimation of currents in the western part of the study region. SPM

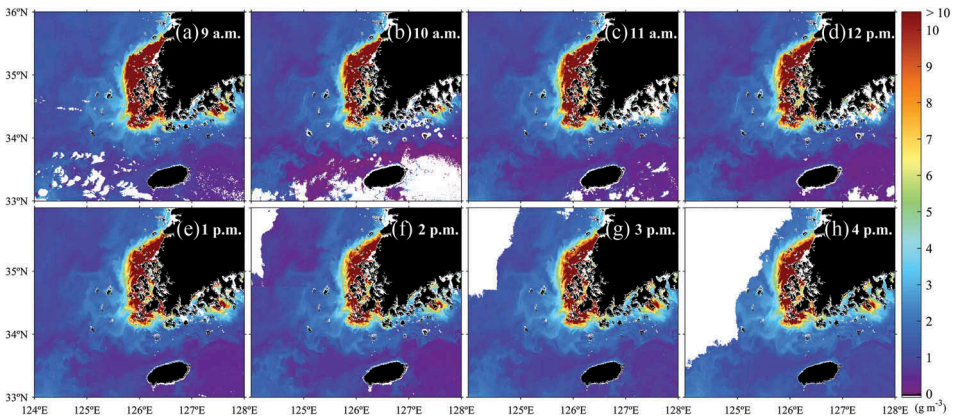


**Figure 2.** Hourly spatial distribution of SPM ( $\text{mg m}^{-3}$ ) from 9 a.m. to 4 p.m. local time (KST, Korea Standard Time) from GOCI data.

concentrations range from relatively high values of 5 to  $10 \text{ g m}^{-3}$  or more in the coastal region to low values of about  $1\text{--}4 \text{ g m}^{-3}$  in the offshore region (Figure 2).

Several algorithms have been developed to quantify the total amounts of SPM in sea water using different sources of satellite data. For the GOCI data, the SPM concentration has been estimated using several algorithms using remote-sensing reflectances centred at approximately 555 nm or through multi-band observations at 490 or 670 nm as well as 555 nm (Moon et al. 2010; Choi et al. 2012). Because we are interested in the spatial movement of SPM over time, an algorithm which uses a single band was selected to avoid the potential problem of less spatial uniformity due to the use of multiband data. We retrieved the SPM concentrations using the GOCI Data Processing System (GDPS), as follows,

$$\text{SPM} = 945.07 R_{rs}^{1.137}, \quad (1)$$

where  $R_{rs}$  is the remote-sensing reflectance in the 555 nm band (Moon et al. 2010).

To investigate the temporal movement of features in the SPM images, we identified SPM fronts using a gradient method. The frontal magnitude  $F$  was obtained from the magnitude of the two-dimensional SPM gradient vector, computed at each grid point of the GOCI data (Park et al. 2007):  $F = |\nabla \text{SPM}|$ . The gradients were formulated with unweighted centred differences using four pixels surrounding the central pixel.

To estimate surface current vectors from hourly SPM images, we applied the well-known MCC method (Emery et al. 1986; Tokmakian, Strub, and McClean-Padman 1990; Bowen et al. 2002; Crocker et al. 2007). Because GOCI images are obtained every hour during the daytime, the SPM values in sequential images may vary due to advective currents as well as changes in the time-varying solar insolation or other in-water situations. Consequently, we normalized the images by subtracting the mean SPM within each window (**A**, **B**) and then divided this by the standard deviation of the SPMs of **A** and **B** by calculating the MCC, as follows,

$$\text{MCC} = \frac{1}{n} \sum_{i,j} \frac{(\mathbf{A}(i,j) - \bar{\mathbf{A}})(\mathbf{B}(i,j) - \bar{\mathbf{B}})}{\sigma_{\mathbf{A}}\sigma_{\mathbf{B}}}, \quad (2)$$

where  $\mathbf{A}$  and  $\mathbf{B}$  are submatrices consisting of SPM with a  $23 \times 23$  window from upcoming and previous images with elapsed time of 1 hour, respectively;  $n$  is the number of instances of  $\mathbf{A}$  or  $\mathbf{B}$ ;  $\bar{\mathbf{A}}$  and  $\bar{\mathbf{B}}$  are the corresponding averages of  $\mathbf{A}$  and  $\mathbf{B}$ ; and  $\sigma_{\mathbf{A}}$  and  $\sigma_{\mathbf{B}}$  are the respective standard deviations of  $\mathbf{A}$  and  $\mathbf{B}$  at the corresponding centre grids of  $i$  and  $j$ .

The vector corresponding to the horizontal movement of SPM was assigned from the centre of the template window,  $\mathbf{A}$ , to a location having a maximum value of the normalized cross-correlation within a  $43 \times 43$  search window. The size of the search window was determined by our determination of the maximum magnitude of tidal currents and sea surface currents in this particular region, where tidal currents are much stronger than residual currents. The MCC method was applied to all pixels in sequential GOCI images captured in one day. Considering the spatial resolution of GOCI and time interval, the maximum and minimum speeds are estimated to  $1.78$  and  $0.14 \text{ m s}^{-1}$ , respectively. The lower limit of the estimated speed of  $0.14 \text{ m s}^{-1}$  corresponds to the speed as a measure of the uncertainty related to the window sizes of MCC method.

For a given template window, there are likely many displacements yielding correlation coefficients ( $r$ ) that are within the confidence limits of the maximum correlation. We estimated the confidence range by taking into consideration of degree of freedom of template window size based on the previous methods (Emery and Thomson 1998; Emery, Fowler, and Clayson 1992). As a result, the limit of the insignificant  $r$  was very small by 0.088 within 95% confidence level.

## 2.2. Numerical model for surface current

The coastal area of the study region is well known for very strong tidal currents due to its shallow depth, complicated coastline, a number of small islands, and other factors. In the literature, there are no reports of dominant oceanic geostrophic or quasi-geostrophic current systems west of Korea in spring, except for the tidal currents in the study region. The mean surface current is likely to be negligible as compared with strong tidal currents during the study period. The Yellow Sea Warm Current, as a typical oceanic warm current in the Yellow Sea appearing in winter only, penetrates from south of Jeju Island to the northwest along a deep channel of the Yellow Sea; however, it deviates far west from the coastal zone (Chen et al. 1994; Ichikawa and Beardsley 2002). As another current system, the Jeju warm current with a speed of  $0.05\text{--}0.4 \text{ m s}^{-1}$  appears strong along the northern coast of Jeju Island in the Jeju Strait (Lie et al. 2000; Lie et al. 2001). However, it appears mainly in summer, while the study period was in the spring. The non-tidal currents in the region depend on the season. Coastal currents west of Korea flow in different directions, i.e. southward in winter and northward in summer, due to different mechanisms (Naimie, Blain, and Lynch 2001). Researchers have not examined the coastal current in April, i.e. during the study period.

Therefore, we used tidal and wind-induced current vectors from a numerical model to compare with currents estimated from satellite data. To simulate the tidal currents, a 3D finite-element numerical tide model, the Semi-implicit Eulerian–Lagrangian Finite Element, was applied to a broad region covering the entire Yellow Sea and the East China Sea. The model was forced with tidal constituents of periods less than a month at the open boundaries (Byun and Cho 2009). The model has variable grid spacing with



very small elements (0.1117 m) near the coast and moderately sized elements (11.17 km in maximum) in the offshore region. Surface current vectors from the numerical model with atmospheric input, such as air pressure and near-surface wind field, were interpolated onto  $500 \times 500$  m GOCI grids for comparison with the currents estimated from SPM data. As atmospheric forcing, wind data and air pressure of Global Data Assimilation and Prediction System of Korea Meteorological Administration were given into the numerical model (Park and Hong 2007).

To validate the model simulation of tide and surface currents, hourly surface elevation data measured by tide gauges were obtained from seven locations near Jeju Island (red dots in Figure 1(b)). Harmonic analysis was performed on the observations and on model surface elevation at these locations, and the reconstructed tidal signals were compared. The overall RMS tidal surface elevation difference, averaged over the seven stations, was 0.198 m. We use this value and scaling arguments, described below, to characterize the uncertainty in model currents. Assuming frictionless non-rotating tidal dynamics, the momentum balance  $\frac{\partial u}{\partial t} = -g \frac{\partial \eta}{\partial x}$  is scaled using the RMS elevation difference ( $\eta_{\text{RMS}}$ ) and the unknown velocity RMS difference ( $U_{\text{RMS}}$ ) as the elevation and velocity scales, the tidal period ( $T$ ) as the timescale, and the tidal wavelength ( $\lambda$ ) as the length scale to get  $U_{\text{RMS}} \approx \frac{g \eta_{\text{RMS}} T}{\lambda}$ , which can be combined with the expression for the shallow water wave phase speed ( $c = \frac{\lambda}{T} = \sqrt{gH}$ ) to obtain  $u_{\text{RMS}} = \left(\frac{g}{H}\right)^{-0.5} \eta_{\text{RMS}}$ , where  $H$  is the water depth and  $g$  is the gravitational acceleration ( $9.8 \text{ m}^2 \text{ s}^{-1}$ ). Using  $\eta_{\text{RMS}} = 0.198 \text{ m}$  and  $H = 100 \text{ m}$  gives  $u_{\text{RMS}} = 0.062 \text{ m s}^{-1}$  as a measure of the model tidal current uncertainty.

### 2.3. Validation of satellite-derived surface currents

We obtained mean currents in the study region from the climatological database of global near-surface currents from the drifter programme of the Atlantic Oceanographic and Meteorological Laboratory (AOML) of the National Oceanic and Atmospheric Administration. This database contains the annual mean vectors of the near-surface currents as calculated from satellite-tracked drifters on a  $0.5^\circ \times 0.5^\circ$  grid (Lumpkin and Johnson 2013). We also used *in-situ* data from a surface drifter passing eastward through the Jeju Strait between Jeju Island and the southern coast of Korea from 1 to 10 April 2011, corresponding to the same month of the study period.

The similarities of the satellite-derived currents and the model tidal currents were quantified by comparing the tidal ellipse parameters of the two current products. Based on the method developed by Park, Woo, and Ryu (2012), an elliptic equation was applied to the periphery of the current vectors to determine the lengths of the major and minor axes, the degree of eccentricity, and the tilting angle of the tidal ellipse.

## 3. Results

### 3.1. Spatial shift of SPM fronts

The sequential GOCI images in Figure 2 depict the spatial movements of SPM over time, particularly at pixels with large horizontal gradients in SPM. To demonstrate the movements clearly, we estimated the spatial gradients of the SPM concentrations and used

this magnitude for the SPM frontal values. The frontal values were  $0.2 \text{ g m}^{-3} \text{ km}^{-1}$  or higher (Figure 3(a,b)), but the spatial movements were difficult to discriminate in only the frontal images. For a better visualization of the spatial structure, SPM fronts were defined as places with high frontal gradient values greater than  $0.1 \text{ g m}^{-3} \text{ km}^{-1}$ , as shown in Figure 3(c,d). For each SPM gradient image, a binary image was created whereby frontal and non-frontal pixels were labelled with 1 and 0, respectively. The subtraction of two successive binary images (e.g. Figure 3(d) minus Figure 3(c)) results in an image in which pixel values of 1 indicate frontal pixels in the second image that were not fronts in the first, and values of  $-1$  indicate frontal pixels in the first image that were not fronts in the second. The difference image (Figure 3(e)) shows bands of  $\pm 1$ , which can be used to infer the horizontal shift of the SPM fronts (from the blue pixels towards the red pixels in Figure 3(e)). The consistent shift of the SPM fronts, generally to the south, suggested spatial movement of the SPM due to the effect of surface currents. For

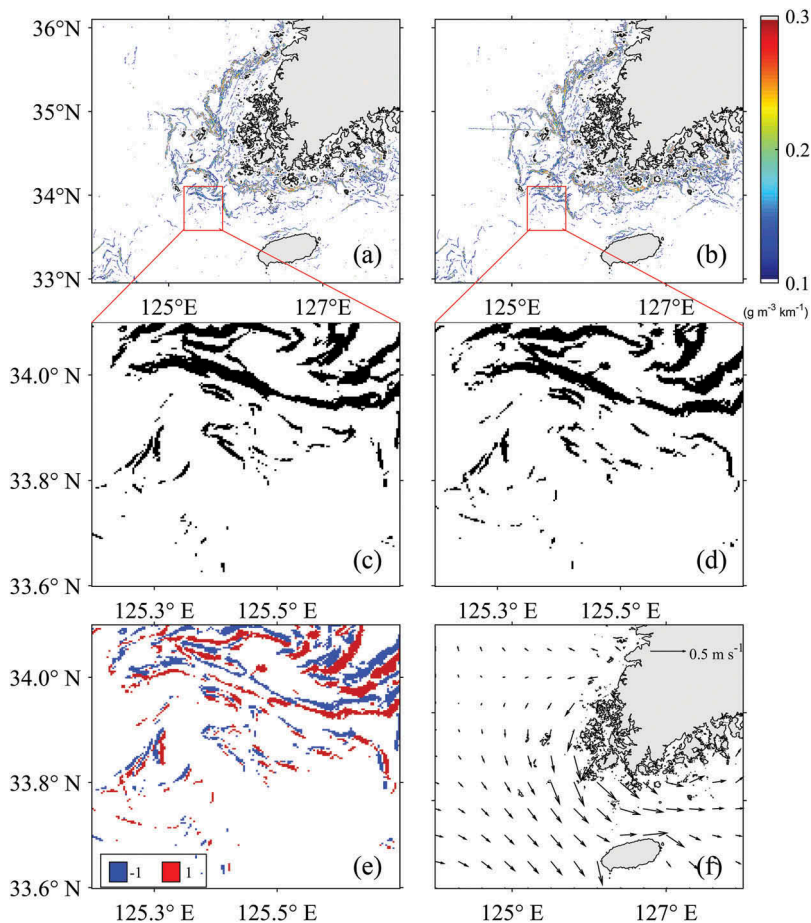


**Figure 3.** Spatial distribution of SPM fronts at (a) 1 p.m. and (b) 2 p.m., (c) and (d) enlarged features from (a) and (b) when applying a threshold for SPM fronts, (e) difference between (c) and (d) representing the movement of SPM fronts to the southwest, and (f) tidal current vectors at 1 p.m. from the numerical tidal model.

comparison, tidal currents from the numerical model over the period 1–2 p.m., corresponding to Figure 3(a,b), are generally southward, suggesting that the observed frontal displacements are largely due to advection by tidal currents.

### 3.2. Quality control of the estimated current

Many current vectors estimated using the MCC method are clearly inaccurate in terms of either the magnitude or direction. Therefore, it is necessary to develop a procedure for such erroneous vectors to be objectively screened out through a quality-control procedure.

First, we applied a threshold to the  $r$  ( $<0.7$ ) between pattern windows and search windows in sequential SPM images in order to reject statistically insignificant current vectors, as shown in the flow diagram in Figure 4. The second criterion was the  $p$ -value associated with the maximum  $r$  between the two windows. Windows for which the  $r$  had high  $p$  values ( $>0.05$ ) were excluded from further processing.

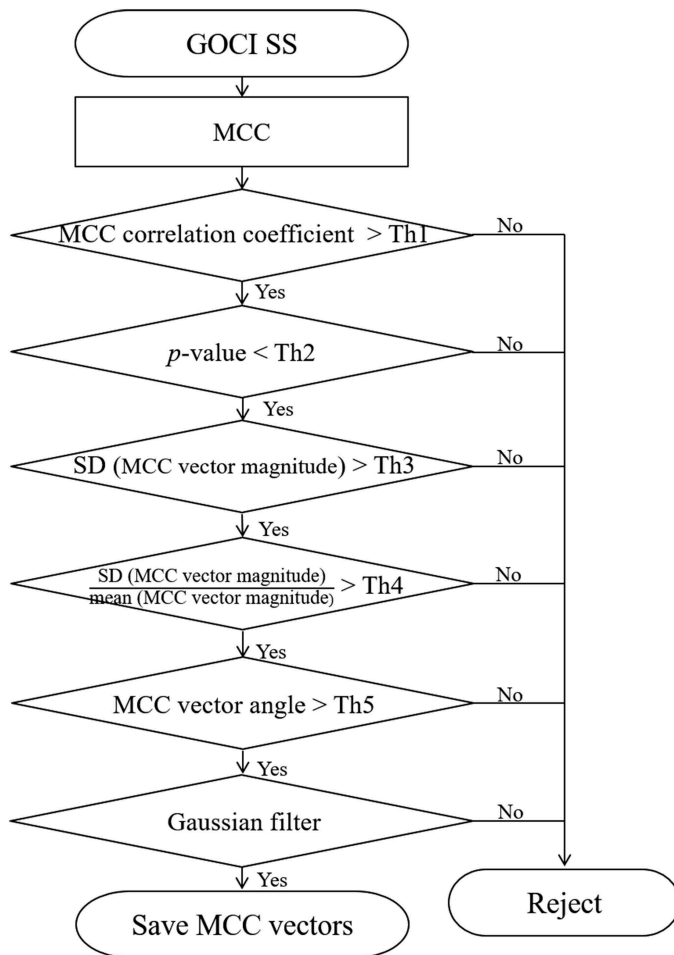
Next, we used a rejection scheme based on spatial uniformity of the current speeds with the standard deviation ( $\sigma$ ,  $>0.4$ ) within a window of  $15 \times 15$ . Because we are interested in a mesoscale current field, a relatively large window was applied. The  $\sigma$  normalized to a mean value ( $\mu$ ),  $\sigma \mu^{-1}$ , was then considered. When we applied a normalized threshold of 0.8, the overall current vectors with higher spatial randomness than those in the neighbouring fields were adequately eliminated. The spatial uniformity of the derived current vectors was also tested by implementing a criterion of a high randomness of angle ( $>20^\circ$ ) to reject poor vectors. Finally, we applied a Gaussian filter over wind vectors within a  $3 \times 3$  window to reduce the random velocity field.

Figure 5(h–n) show the currents passing the above quality-control procedure in comparison to the unscreened current vectors in Figure 5(a–g). Erroneous MCC vectors with random current directions appeared mainly over the southern regions ( $<34^\circ$  N) where SPM is very low (less than  $1 \text{ g m}^{-3}$ ). After the application of the quality-control procedure, most of the erroneous vectors disappeared, as shown in Figure 5(h–n).

### 3.3. Comparison with numerical model currents

The accuracies of the retrieved surface currents were assessed in comparison with the tidal currents from the numerical model. The currents were derived at every grid point ( $997 \times 1332$ ) of sequential GOCI images and were compared with model tidal currents interpolated to the GOCI grid. Figure 6(a) presents a comparison of the binned averages of eastward MCC speeds ( $u_{\text{MCC}}$ ) with those of the tidal currents ( $u_{\text{Model}}$ ), where the error bars represent the standard deviations of the eastward component of MCC speeds within each current speed bin. Both of the eastward and northward components of the MCC current vectors show a good relationship with the tidal current (Figure 6(b)).

Figure 6(c) shows a comparison of the binned averages of MCC speeds ( $U_{\text{MCC}}$ ) with those of the tidal currents ( $U_{\text{Model}}$ ). The estimated current speeds show a linear relationship with the model currents in the range of  $0.30\text{--}0.60 \text{ m s}^{-1}$  with a  $r$  of about 0.86 ( $p = 1.35e^{-15}$  within a 95% confidence interval). However, the current retrievals exhibited a considerable positive bias in the low range (tidal currents



**Figure 4.** Flow diagram of quality-control procedure to eliminate poor current vectors from the MCC results, where standard deviation is denoted as SD and a series of different thresholds is denoted as Th1–Th5.

$<0.2 \text{ m s}^{-1}$ ). In this range, bin-averaged MCC current speeds were approximately constant at about  $0.2 \text{ m s}^{-1}$ . This might be originated from the positive mean speeds by deriving absolute values of current vectors, from the effect of oceanic mean currents, or from other error sources. In the high tidal current range of  $0.6\text{--}1.2 \text{ m s}^{-1}$ , MCC current speeds were significantly low in comparison to the model tidal currents. The large error bars in Figure 6(c) are attributed to the small number of matchup points. The inverse relationship apparent in Figure 6(c) for model currents greater than  $0.6 \text{ m s}^{-1}$  suggests that as the tidal currents increased, the MCC currents tended to decrease. This will be discussed further by examining the tidal frontal zone in the following section.

In contrast to the discrepancies in current speed, the directions of the estimated current vectors in Figure 6(d) were in good agreement with those of the tidal currents with a remarkable linear relationship with a slope of 1.095 ( $r = 0.99$ ,  $p < 10^{-20}$  within a

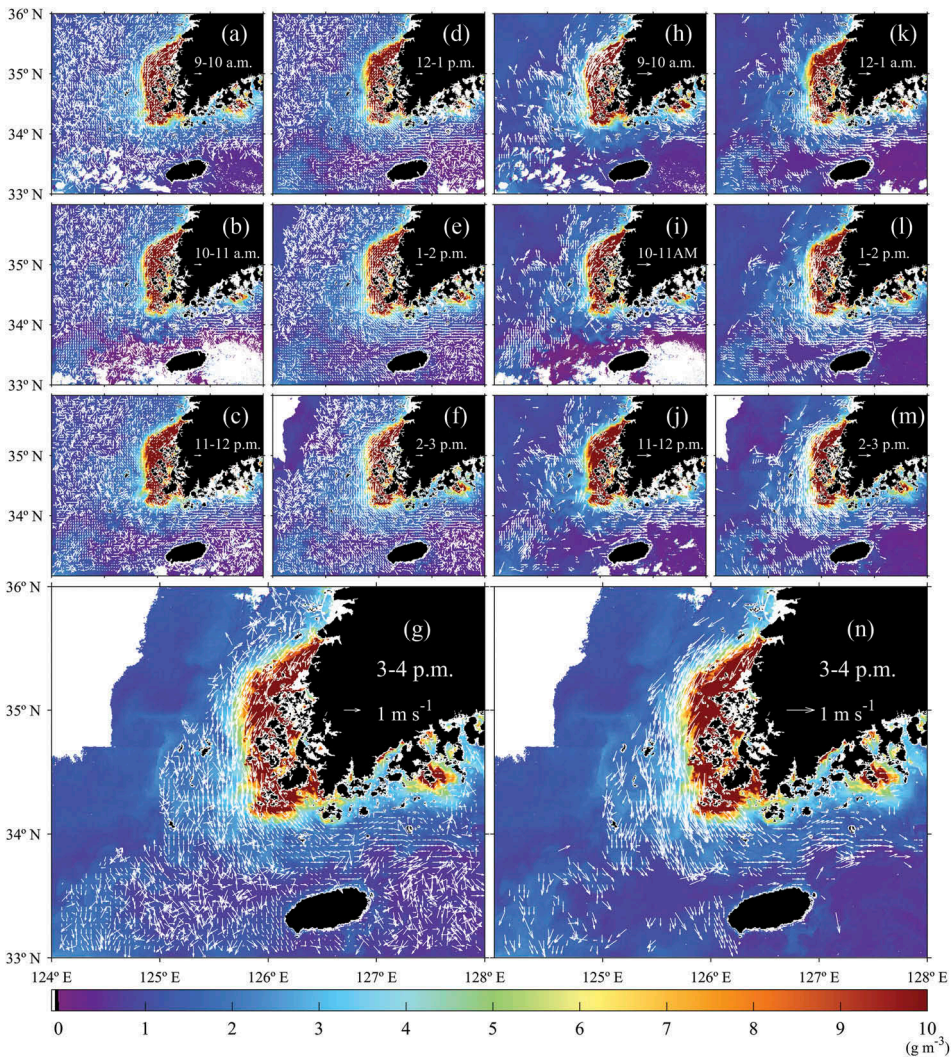


**Figure 5.** Spatial distribution of the estimated current vectors over a mean SPM image from 9 a.m. to 4 p.m. Figure parts (a)–(g) before and (h)–(n) after the quality-control process, where each SPM image is an average of two images with an hourly interval (subsampling 1/15).

95% confidence interval). This implies that the directions of the estimated currents were properly determined in spite of the poor estimation of the tidal current speeds in the high current regimes (Figure 6(d)).

### 3.4. Ellipses from time-varying current vectors and tilting angles

Considering that the study region is well known for its strong tidal currents, the time-varying tidal current vectors showed conspicuous ellipses, as shown in Figure 7(a). The tidal ellipse orientation ranged widely from  $0^\circ$  to  $180^\circ$  over the study region. The initial vectors, marked by the black arrow, rotated clockwise or counterclockwise with time, as



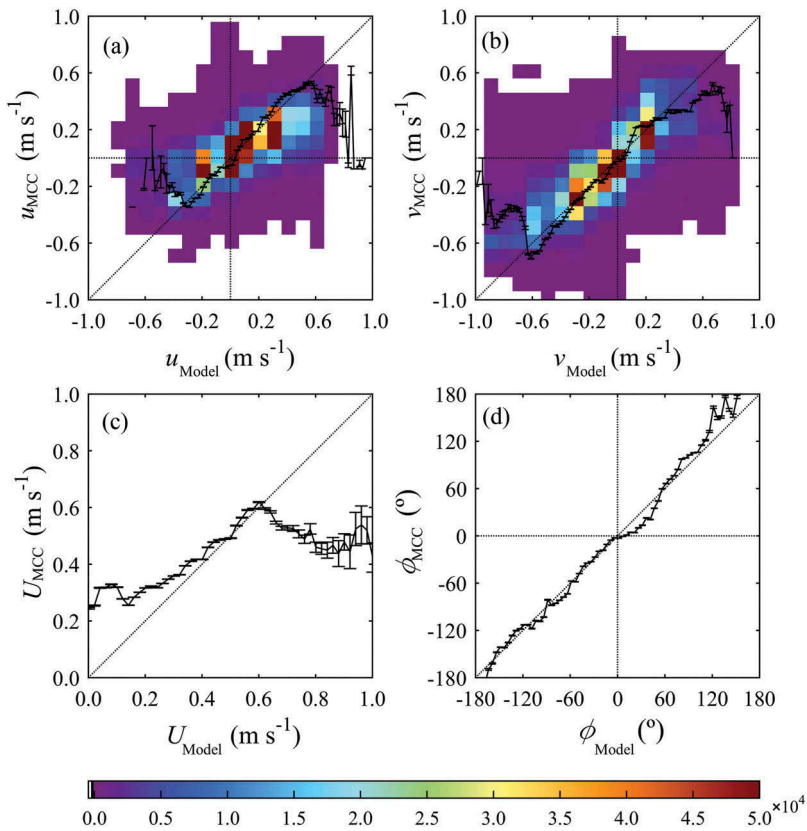


**Figure 6.** Comparison of (a) eastward ( $u_{MCC}$ ) and (b) northward ( $v_{MCC}$ ) magnitude of the estimated vectors with respect to currents from a numerical model and (c) the magnitude and (d) angle of the estimated current vectors with respect to those of the numerical model.

indicated in the monotonically changing grey colours (Figure 7(a)). The shapes of the tidal ellipses were diverse, such as a nearly circular ellipse in the southwestern part, moderately elongated ellipses, or highly elongated ellipses composed of progressive and retrogressive movements (Figure 7(a)).

If the erroneous current vectors were properly filtered through the quality-control procedure, the estimated vectors would have an ellipse similarly to the tidal ellipse. To test this, a procedure similarly to that used with the tidal currents was applied to the hourly varying current vectors from satellite images. We estimated the orientation angles of the ellipse traced out by the estimated vectors, as denoted in the upper left corner of Figure 7(b), using the elements of the ellipse based on the method of Park, Woo, and Ryu (2012). Figure 7(b) shows a comparison between the orientation angles of the model tidal ellipses and those of the ellipses estimated from the hourly current vectors at every grid point. The orientation angles of the estimated currents were obtained from the eight available hourly satellite images, although this was somewhat insufficient to compose a full cycle of the semidiurnal tide. Regardless of the deficiency of the vectors for a complete ellipse, the estimated orientation angles showed a remarkable linear correlation to those of the tidal vectors with a high  $r$  of nearly 0.939

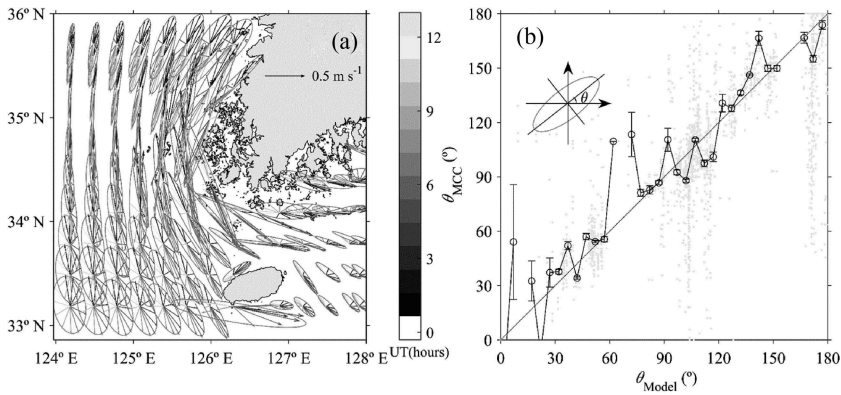


**Figure 7.** (a) Tidal ellipses of time-varying tidal current vectors during a cycle of the principal lunar semi-diurnal tide and (b) comparison of the tilting angles of ellipses from the estimated current vectors ( $\theta_{MCC}$ ) and tidal current vectors ( $\theta_{Model}$ ).

( $p = 1.90 \times 10^{-15}$ ). Thus, it is concluded that the directions of the SPM movements were statistically significant with respect to the direction of the dominant currents.

### 3.5. Characteristics of the angular velocity of the current vectors

If the MCC current vectors were satisfactorily filtered out through the quality-control procedure, the directions of the currents should be similar to those of major tidal currents over time under the condition of negligible mean current as mentioned earlier. The Ekman drift was evaluated to be small ( $0.03\text{--}0.05 \text{ m s}^{-1}$ ) according to our estimation; therefore, we disregarded the weak effects of wind field or other general oceanic currents in the comparison of the angular velocity and took the tide into consideration as a primary contributor to the estimated currents.

To calculate the rotational angular velocity of the tidal current vectors and the estimated current vectors, the differences at each grid were obtained by subtracting the angle of the tidal vectors of the first SPM image at 9 a.m. from that of the following hourly vectors. The temporal change rates of the current directions were then derived for the rotational angular velocity ( $^{\circ} \text{ hour}^{-1}$ ) of the current vectors by means of linear least-squared fitting. There were two types of trends, cyclonic rotation and anticyclonic rotation, in the study region (Figure 8(a)). Most of the southwestern portion showed a clockwise rotation with negative values of about  $-30^{\circ} \text{ hour}^{-1}$ , which corresponded to the semi-diurnal tide. This feature was reversed to anticlockwise rotation in the northern and southeastern region with angular velocities of approximately  $30^{\circ} \text{ hour}^{-1}$ .

If the retrieved currents represent the tidal currents comparatively well, the quality-controlled estimated current vectors should be similar to the rotation of the tidal current vectors. Figure 8(b) shows the spatial distribution of the angular velocities of the satellite-estimated current vectors at every grid. Due to the rejection schemes of the quality-control process and the poor cloud coverage, numerous

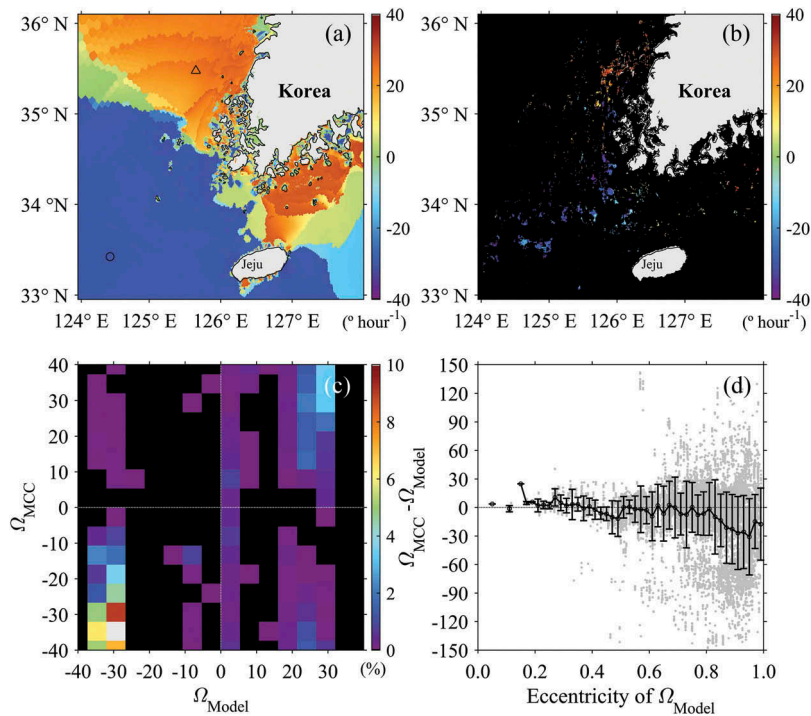


**Figure 8.** Distribution of the angular velocities of the current vectors from (a) the tidal model and (b) the GOCI SPM data, (c) comparison of (a) and (b), where the colours represent the number density of 2D histogram, and (d) differences in the angular velocities as a function of the eccentricity of the tidal ellipse composed of tidal current vectors.

pixels were eliminated from the calculation, particularly in the region of anticlockwise rotation. Nevertheless, the remaining angular velocities are distributed quite similarly to the results from the model tidal currents overall, as shown in Figure 8(b). This coincidence suggests that the MCC method can adequately resolve the tidal evolution of current vector direction.

For a more quantitative approach, we compared angular velocities between the estimated currents and the model tidal currents in a 2D histogram (Figure 8(c)). The overall pattern indicated that a large number of MCC angular velocities occurred at  $\pm 30^{\circ}$  hour $^{-1}$ , corresponding to the angular velocity of semi-diurnal tidal currents. However, some erratic points were found to be concentrated near a  $\Omega_{MCC}$  value of  $0^{\circ}$  hour $^{-1}$  when  $\Omega_{Model}$  was  $30^{\circ}$  hour $^{-1}$  (Figure 8(c)). Such errors appeared to estimation errors which arose in cases of highly elongated tidal current ellipses, as shown in Figure 7(a). The mean differences of  $\Omega_{MCC} - \Omega_{Model}$  were near zero in most ranges of eccentricity ( $< 0.9$ ); however, pixels with large differences were broadly distributed as scattered points at high levels of eccentricity ranging from 0.9 to 1 (Figure 8(d)). Thus, it is concluded that the elliptic characteristics of surface currents are difficult to investigate at regions with high eccentricity of the elongated tidal ellipse.



### 3.6. Characteristics of the estimated currents in the tidal frontal zone

In contrast to the positive correlation between MCC and model tidal currents (or tidal plus Ekman currents) at current speeds between 0.2 and 0.6 m s<sup>-1</sup>, the estimated currents demonstrated a somewhat negative correlation and underestimation at current speeds of greater than 0.6 m s<sup>-1</sup> (Figure 6). What caused such a relationship? First, we investigated where the pixels with poor correlations (>0.6 m s<sup>-1</sup>) were located in the study region (Figure 9). Most of the scattered points were concentrated not in the offshore region but near the coastal region off Korea. Apparently, this region corresponds to the tidal frontal zone, where tidal currents were exceedingly strong (Lie 1989). Therefore, it was hypothesized that the vigorous vertical tidal mixing process would be dominant over horizontal advection in the surface SPM budget. If the considerable errors of the estimated currents occurred due to tidal mixing in response to spring-to-neap or neap-to-spring currents within the tidal front zone, the temporal variations of the spatial extents of the locations with large errors (Figure 9) would be similar to those of the tidal front zone.

As expected, the percentage ratio (%) of the spatial extents of the large errors to the area of clear sky revealed characteristic temporal variations with time (Figure 9(h)). This was much higher, by 6%, at 9 a.m. and then abruptly began to decrease to a small fraction of about 0.0061% (0.9253 km<sup>2</sup>) from 10 a.m., reaching a minimum of 0.0039% (0.5552 km<sup>2</sup>) at 11 a.m. (Figure 9(h)). The decreasing trend of the extent was, in turn, reversed and became an increasing trend after 11 a.m., lasting until 3 p.m. If this trend is meaningfully related to the magnitude of the tidal currents, the areas of the dots should coincide with those of the tidal frontal zone.

To illustrate its relationship, a tidal frontal zone was defined as a region with a small Simpson index  $H U_{\max}^{-3}$  of less than 2.2 (Simpson and Hunter 1974). Figure 10 shows the results of the index as estimated with the maximum tidal current speed ( $U_{\max}$ ) and water

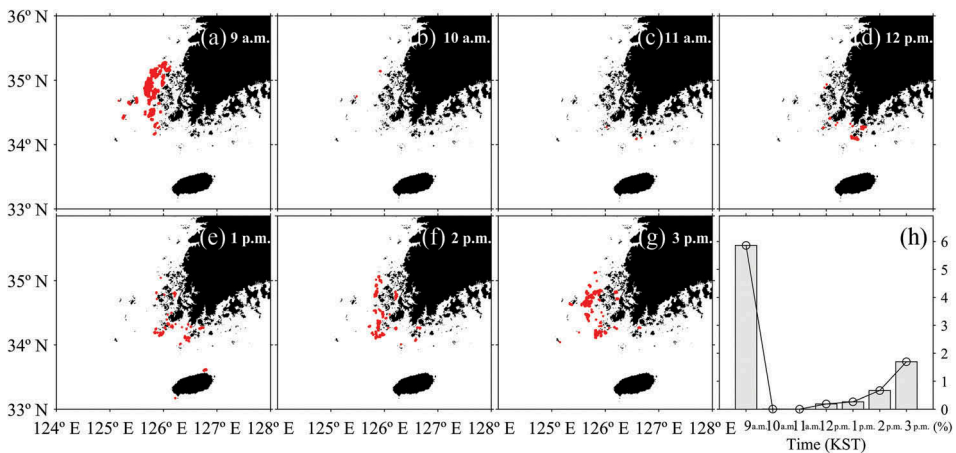


**Figure 9.** Spatial distribution of points with large errors for high tidal currents greater than 0.6 m s<sup>-1</sup> from (a) 9 a.m. to (g) 3 p.m., and (h) hourly variations of the normalized percentage of erroneous points to the number of clear-sky pixels, where the red (blue) dots show a negative (positive) correlation with the tidal current speeds.

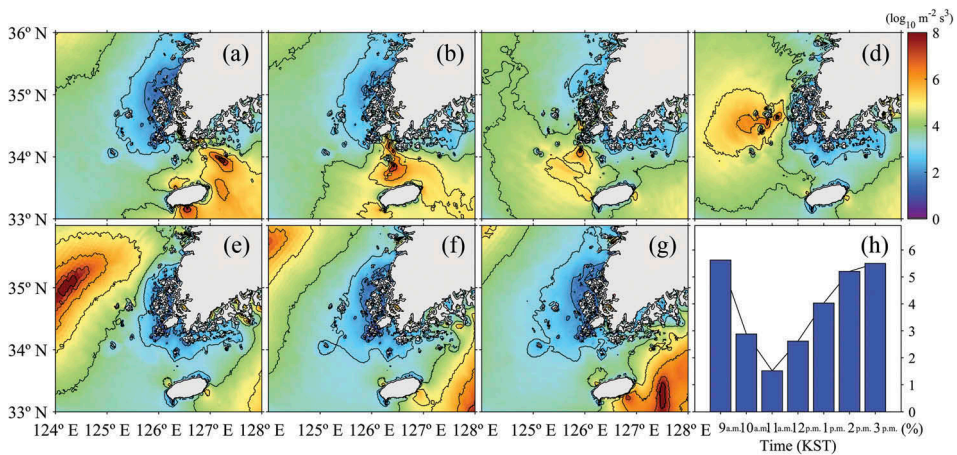


**Figure 10.** Distribution of the tidal front index ( $\log_{10} H U^{-3}$ ) estimated from the tidal current speed and water depth.

depth ( $H$ ) using the numerical tidal model. The index was high, reaching 5 in the offshore region, while it was very low at less than 2 in the coastal region. The distribution of the frontal zone ( $<2.2$ ) presented temporal variations of its areal coverage, which was to some extent comparable to the variation of areas with large inconsistencies in the estimated currents, as shown in Figure 10(h). This value was appreciably reduced to a minimum of about 1.52 at 11 a.m., which was in accordance with the temporal changes in the numbers of pixels with high tidal errors in Figure 10(h). That is, the estimation errors were proportional to the magnitudes of the tidal currents over time. Therefore, it is inferred that as the tidal current becomes stronger, the estimated currents will be more likely to contain large errors and show a different relationship due to the vigorous vertical mixing of the SPM in the frontal zone.

To test this conjecture, we investigated the characteristics of the estimated current vectors within the tidal frontal region (Simpson index  $<2.2$ ). For the purpose of understanding these characteristics, we did not apply a quality-control process to individual vectors. At values exceeding  $0.6 \text{ m s}^{-1}$ , the MCC current speeds exhibited a negative relationship with regard to the tidal current magnitude at a rate of  $-0.2981$  (Figure 6(c)). This signifies that the MCC currents were no longer strong in proportion to the strength of the tidal currents in the frontal zone. Rather, they showed an obvious inverse trend. Therefore, the MCC method is regarded as not always appropriate in the tidal frontal zone when used to determine the actual currents, as active vertical tidal mixing resulting in a high re-suspension of sediment or particulate matter modifies the signal of the horizontal movement of SPM.

One intriguing finding in the tidal frontal zone is that the directions of the current vectors remained unchanged in spite of the obvious decrease in the trend of the estimated speeds (Figure 6(d)). This suggests that the predominant vertical mixing within the tidal front zone prevented an increase in the horizontal current speeds. Nevertheless, the surface flow continued to propagate towards the main direction of the tidal current vectors at an inclination of 1.021, suggesting that it was highly probable that our fundamental assumption of the MCC current method itself with regard to horizontal movement could be violated in the frontal zone.

## 4. Discussion

### 4.1. Potential cause of underestimated current

It was noted that the estimated current speeds tended to be underestimated at tidal current speeds above about  $0.6 \text{ m s}^{-1}$ . What mechanism is related to the critical speed limit of  $0.6 \text{ m s}^{-1}$ ? The overall distribution of the surface SPM concentration greatly increased towards the shallow water region with an inverse relationship of  $-1.04$  (Figure 11(a)). The shallow zone coincided with the tidal frontal zone, where relatively high tidal currents dominated. Figure 11(b) shows the variations of the mean SPM as a function of the tidal current speed, where the error bar is the standard deviation of SPM for the entire study region in all GOCI images from 9 a.m. to 4 p.m. The mean SPM values increased gradually from 2 to  $3 \text{ g m}^{-3}$  when the tidal current value was less than  $0.4 \text{ m s}^{-1}$  but increased rapidly from  $1.80 \text{ g m}^{-3}$  at high tidal currents for tidal currents in the range of  $0.31\text{--}0.81 \text{ m s}^{-1}$  (Figure 11(b)). Beyond this current speed ( $>1.2 \text{ m s}^{-1}$ ), they were nearly constant at approximately  $13.3 \text{ g m}^{-3}$ , although the hourly variations of SPM, shown in colour in Figure 11(b), depended on the magnitude of the tidal currents.

The satellite-observed mean SPM did not continue to increase in the frontal zone irrespective of the magnitude of the tidal currents. The current speed beginning with a constant SPM was detected at  $0.65\text{--}0.70 \text{ m s}^{-1}$ , which was close to the critical speed according to the tidal current and the Ekman drift at about  $0.6 \text{ m s}^{-1}$ , as mentioned earlier in Figure 6(c). This suggests some influence of active tidal mixing on the re-suspension or disappearance of the satellite-observed SPM concentration at/near the sea surface. Such a characteristic mean pattern of the SPM distribution appears to be responsible for the speed limit in the study region.

### 4.2. Potential cause of overestimated current

Although we considered the effect of the tidal current as well as the Ekman drift due to the wind field, the estimated current speeds were still significantly high for weaker currents of less than  $0.2 \text{ m s}^{-1}$ , as shown in Figure 6(c). According to our estimation, the Ekman drift was small ( $0.03\text{--}0.05 \text{ m s}^{-1}$ ) in terms of its contribution to the total current

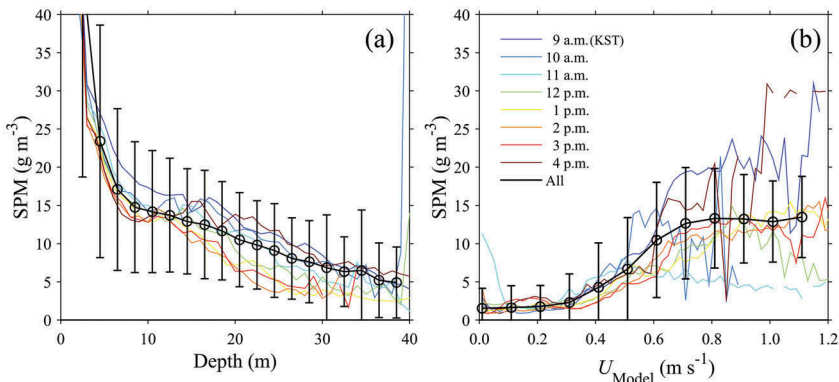


**Figure 11.** Variations of the SPM averaged over the entire study region as a function of (a) the water depth (m) at 9 a.m. and (b) the tidal current ( $\text{m s}^{-1}$ ) from 9 a.m. to 4 p.m.

speed during the study period. One of the potential causes of the overestimation of the retrieved current speeds would be the effect of mean oceanic currents in this region. However, in the literature, there are no reports of dominant oceanic current systems west of Korea, except for the tidal currents in the study region in spring. The mean surface current is likely to be negligible as compared with strong tidal currents in the western coast of Korea during the study period. As described earlier, the Yellow Sea Warm Current deviates far west from the coastal zone in winter (Chen et al. 1994; Ichikawa and Beardsley 2002).

Nevertheless, the systematic positive biases at weak tidal currents ( $<0.2 \text{ m s}^{-1}$ ) in Figure 6(c) are believed to stem from the oceanic currents. To confirm this presumption of similarity between the residual currents and the mean current, we estimated the velocity difference,  $U_{MCC} - U_{Model} (= U_{tide} + U_{wind})$ , and compared the results with the mean current speeds based on satellite-tracked drifters managed by AOML (<http://www.aoml.noaa.gov/>). As shown in Figure 12(a,b), the residual current speeds were less than  $0.2 \text{ m s}^{-1}$ . In Figure 6(c), the positions of the pixels with overestimations at low currents ( $<0.2 \text{ m s}^{-1}$ ) coincided with the regions with high tidal indices greater than 7, which were mostly distributed over the southeastern region, as shown in Figure 10(a,b). Such regions would be most likely related to other currents, apart from tidal currents or the wind drift.

Specifically, relatively high currents ( $>0.15 \text{ m s}^{-1}$ ) were concentrated in the southern regions along  $33.8^\circ \text{ N}$  east of Jeju Island (Figure 12(a)) and were mostly directed towards the east (Figure 12(b)). Features of this type were quite similarly to the mean current

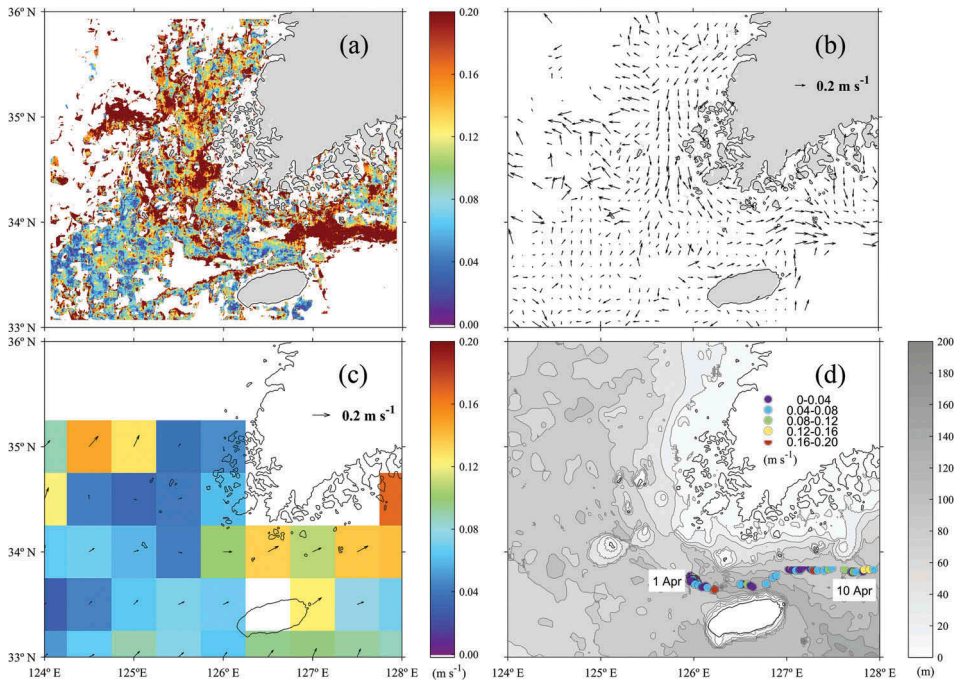


**Figure 12.** (a) Mean magnitudes of the estimated current with the tidal current subtracted from it, (b) its mean vector, (c) long-term averaged drifter-derived current in April, and (d) drifter data from 1 April to 10 April 2011.

pattern in terms of the magnitude and direction, as indicated in Figure 12(c). To confirm the effect of the mean currents, we estimated the surface currents from the satellite-tracked drifter within the study region (Figure 12(d)). The surface drifter passed eastward through the Jeju Strait from 1 to 10 April of 2011. The speeds ( $<0.2 \text{ m s}^{-1}$ ), with the tidal current eliminated through a filtering procedure, were also similarly to the residual currents (Figure 12(b)) and the mean current speeds (Figure 12(c)). Both magnitudes and directions were coincident with the residual currents. Such similarity can explain the overestimations of MCC currents at weak currents ( $<0.2 \text{ m s}^{-1}$ ) with regard to the tidal current speed, answering a question raised in the previous sections.

Thus, it is concluded that the estimated current field provides considerable information about the rapidly changing oceanic currents, including tidal currents and tidal residual currents, the wind-driven Ekman drift, and the density-driven mean currents in this particular region.

## 5. Summary and conclusion

Hourly variations of surface currents were derived from SPM concentration data from GOCI using the MCC method. Although the initial vectors apparently indicated a random surface flow field, the estimated currents represented the actual current field comparatively well after passing through a quality-control procedure. The magnitudes of the retrieved currents were in good agreement with those of the model-simulated currents. However, the good coincidence was limited to low current speeds of less than  $0.6 \text{ m s}^{-1}$ . At relatively high current speeds in excess of  $0.6 \text{ m s}^{-1}$ , the two current vectors revealed considerable errors related to the tidal frontal zone. In contrast, the directions of the estimated current vectors revealed a good linear relationship to those of the tidal currents. The Ekman drift due to wind accounted for approximately 5% ( $0.04\text{--}0.06 \text{ m s}^{-1}$ ) to 18% ( $>0.06 \text{ m s}^{-1}$ ) of the retrieved MCC vectors over the study region. Thus, it should be noted that the role of the wind was negligible where tidal currents was significantly large during the study period.

Relatively large errors in the estimated currents appeared at the tidal frontal zone with a high SPM concentration near the coastal area. Thus, the MCC method for deriving the currents is applicable to regions with moderate SPM concentrations. In addition, the directions of time-varying estimated currents were deflected by following an ellipse of the tidal current vectors with the established hourly changes. However, if the SPM concentrations are inconsequentially small in deep offshore regions, the MCC method cannot be properly utilized to trace the spatial movements of SPM. The number of pixels rejected from the QC procedure showed a quadratic relationship to the Simpson index, as an indicator of the tidal front, implying that researchers should be cautious when using the retrieval method in tidal frontal zones. Thus, the surface flow based on the MCC method as well as other pattern-matching methods should be carefully utilized depending on the local sea conditions, particularly in regions with high randomness of the current field related to diverse forces, such as tides, tidal currents, oceanic currents, wind-induced vertical and horizontal mixing, river flows, atmospheric conditions such as precipitation, and others.



## Acknowledgements

This research was a part of the project titled 'Research for Applications of Geostationary Ocean Color Imager' and partly supported by the project titled 'Long-term change of structure and function in marine ecosystems of Korea' funded by the Ministry of Oceans and Fisheries, Korea. We thank Prof. Byung Ho Choi for allowing us use SELFE data.

## Disclosure statement

No potential conflict of interest was reported by the authors.

## Funding

This work was supported by the Ministry of Oceans and Fisheries of Korea.

## References

- Bowen, M. M., W. J. Emery, J. L. Wilkin, P. C. Tildesley, I. J. Barton, and R. Knewton. 2002. "Extracting Multiyear Surface Currents from Sequential Thermal Imagery Using the Maximum Cross-Correlation Technique." *Journal of Atmospheric and Oceanic Technology* 19: 1665–1676. doi:10.1175/1520-0426(2002)019<1665:EMSCFS>2.0.CO;2.
- Byun, D.-S., and C.-W. Cho. 2009. "Exploring Conventional Tidal Prediction Schemes for Improved Coastal Numerical Forecast Modeling." *Ocean Modelling* 28 (4): 193–202. doi:10.1016/j.ocemod.2009.02.001.
- Chen, C., R. C. Beardsley, R. Limeburner, and K. Kim. 1994. "Comparison of Winter and Summer Hydrographic Observations in the Yellow and East China Seas and Adjacent Kuroshio during 1986." *Continental Shelf Research* 14: 909–929. doi:10.1016/0278-4343(94)90079-5.
- Cho, Y.-K., M.-O. Kim, and B.-C. Kim. 2000. "Sea Fog around the Korean Peninsula." *Journal of Applied Meteorology* 39: 2473–2479. doi:10.1175/1520-0450(2000)039<2473:SFATKP>2.0.CO;2.
- Choi, J.-K., Y. J. Park, J. H. Ahn, H.-S. Lim, J. Eom, and J.-H. Ryu. 2012. "GOCI, the World's First Geostationary Ocean Color Observation Satellite, for the Monitoring of Temporal Variability in Coastal Water Turbidity." *Journal of Geophysical Research* 117: C09004. doi:10.1029/2012JC008046.
- Choi, J.-K., H. Yang, H.-J. Han, J.-H. Ryu, and Y.-J. Park. 2013. "Quantitative Estimation of Suspended Particulate Matter Movements in Coastal Region Using GOCI." *Journal of Coastal Research* 65 (2): 1367–1372. doi:10.2112/SI65-231.1.
- Crocker, R. I., D. K. Matthews, W. J. Emery, and D. G. Baldwin. 2007. "Computing Coastal Ocean Surface Currents from Infrared and Ocean Color Satellite Imagery." *IEEE Transactions on Geoscience and Remote Sensing* 45 (2): 435–447. doi:10.1109/TGRS.2006.883461.
- D'Sa, E. J., R. L. Miller, and B. A. McKee. 2007. "Suspended Particulate Matter Dynamics in Coastal Waters from Ocean Color: Application to the Northern Gulf of Mexico." *Geophysical Research Letter* 34: L23611. doi:10.1029/2007GL031192.
- Emery, W. J., C. Fowler, and C. A. Clayson. 1992. "Satellite-Image-derived Gulf Stream Currents Compared with Numerical Model Results." *Journal of Atmospheric and Oceanic Technology* 9: 286–304. doi:10.1175/1520-0426(1992)009<0286:SIDGSC>2.0.CO;2.
- Emery, W. J., A. Thomas, M. Collins, W. Crawford, and D. Mackas. 1986. "An Objective Method for Computing Advective Surface Velocities from Sequential Infrared Satellite Images." *Journal of Geophysical Research* 91 (C11): 12865–12878. doi:10.1029/JC091iC11p12865.
- Emery, W. J., and R. E. Thomson. 1998. *Data Analysis Methods in Physical Oceanography*. Great Britain: Pergamon Press.

- Findlay, S., M. Pace, and D. Lints. 1991. "Variability and Transport of Suspended Particulate Matter, Particulate and Dissolved Organic Carbon in the Tidal Freshwater Hudson River." *Biogeochemistry* 12: 149–169. doi:10.1007/BF00002605.
- Ichikawa, H., and R. C. Beardsley. 2002. "The Current System in the Yellow and East China Seas." *Journal of Oceanography* 58 (1): 77–92. doi:10.1023/A:1015876701363.
- Kamachi, M. 1989. "Advective Surface Velocities Derived from Sequential Images for Rotational Flow Field: Limitations and Applications of Maximum Cross-Correlation Method with Rotational Registration." *Journal of Geophysical Research* 9 (C12): 18227–18233. doi:10.1029/JC094iC12p18227.
- Kelly, K. A. 1989. "An Inverse Model for Near-Surface Velocity from Infrared Images." *Journal of Physical Oceanography* 19: 1845–1864. doi:10.1175/1520-0485(1989)019<1845:AIMFNS>2.0.CO;2.
- Lee, H. J., and S. K. Chough. 1989. "Sediment Distribution, Dispersal and Budget in the Yellow Sea." *Marine Geology* 87 (2–4): 195–205. doi:10.1016/0025-3227(89)90061-3.
- Lee, H. J., S. K. Chough, K. S. Jeong, and S. J. Han. 1987. "Geotechnical Properties of Sediment Cores from the Southeastern Yellow Sea: Effects of Depositional Processes." *Marine Geotechnology* 7 (1): 37–52. doi:10.1080/10641198709388204.
- Leese, J. A., C. S. Novak, and B. B. Clark. 1971. "An Automated Technique for Obtaining Cloud Motion from Geosynchronous Satellite Data Using Cross Correlation." *Journal of Applied Meteorology* 10: 118–132. doi:10.1175/1520-0450(1971)010<0118:AATFOC>2.0.CO;2.
- Lie, H. J. 1989. "Tidal Fronts in the Southeastern Hwanghae (Yellow Sea)." *Continental Shelf Research* 9 (6): 527–546. doi:10.1016/0278-4343(89)90019-8.
- Lie, H.-J., C.-H. Cho, J.-H. Lee, S. Lee, and Y. Tang. 2000. "Seasonal Variation of the Cheju Warm Current in the Northern East China Sea." *Journal of Oceanography* 56 (2): 197–211. doi:10.1023/A:1011139313988.
- Lie, H. J., C. H. Cho, J. H. Lee, S. Lee, Y. Tang, and E. Zou. 2001. "Does the Yellow Sea Warm Current Really Exist as a Persistent Mean Flow?" *Journal of Geophysical Research* 106 (C10): 22199–22210. doi:10.1029/2000JC000629.
- Lumpkin, R., and G. C. Johnson. 2013. "Global Ocean Surface Velocities from Drifters: Mean, Variance, El Niño–Southern Oscillation Response, and Seasonal Cycle." *Journal of Geophysical Research* 118: 2992–3006. doi:10.1002/jgrc.20210.
- Martin, J. M., and M. Meybeck. 1979. "Elemental Mass-Balance of Material Carried by Major World Rivers." *Marine Chemistry* 7 (3): 173–206. doi:10.1016/0304-4203(79)90039-2.
- Matthews, D. K., and W. J. Emery. 2009. "Velocity Observations of the California Current Derived from Satellite Imagery." *Journal of Geophysical Research* 114: C08001. doi:10.1029/2008JC005029.
- Moon, J. E., Y. H. Ahn, J. H. Ryu, and P. Shanmugam. 2010. "Development of Ocean Environmental Algorithms for Geostationary Ocean Color Imager (GOCI)." *Korean Journal of Remote Sensing* 26: 189–207.
- Moon, J.-H., N. Hirose, and J.-H. Yoon. 2009. "Comparison of Wind and Tidal Contributions to Seasonal Circulation of the Yellow Sea." *Journal of Geophysical Research* 114: C08016. doi:10.1029/2009JC005314.
- Naimie, C. E., C. A. Blain, and D. R. Lynch. 2001. "Seasonal Mean Circulation in the Yellow Sea—A Model-Generated Climatology." *Continental Shelf Research* 21: 667–695. doi:10.1016/S0278-4343(00)00102-3.
- Ninnis, R. M., W. J. Emery, and M. J. Collins. 1986. "Automated Extraction of Pack Ice Motion from Advanced Very High Resolution Radiometer Imagery." *Journal of Geophysical Research* 911 (C9): 10725–10734. doi:10.1029/JC091iC09p10725.
- Park, H., and S.-Y. Hong. 2007. "An Evaluation of a Mass-Flux Cumulus Parameterization Scheme in the KMA Global Forecast System." *Journal of the Meteorological Society of Japan* 85 (2): 151–169. doi:10.2151/jmsj.85.151.
- Park, K.-A., D. S. Ullman, K. Kim, J. Y. Chung, and K.-R. Kim. 2007. "Spatial and Temporal Variability of Satellite-Observed Subpolar Front in the East/Japan Sea." *Deep Sea Research* 54 (4): 453–470. doi:10.1016/j.dsr.2006.12.010.

- Park, K.-A., H.-J. Woo, and J.-H. Ryu. 2012. "Spatial Scales of Mesoscale Eddies from GOCI Chlorophyll-A Concentration Images in the East/Japan Sea." *Ocean Science Journal* 47 (3): 347–358. doi:[10.1007/s12601-012-0033-3](https://doi.org/10.1007/s12601-012-0033-3).
- Simpson, J. H., and J. R. Hunter. 1974. "Fronts in the Irish Sea." *Nature* 250 (5465): 404–406. doi:[10.1038/250404a0](https://doi.org/10.1038/250404a0).
- Tokmakian, R., P. T. Strub, and J. McClean-Padman. 1990. "Evaluation of the Maximum Cross-Correlation Method of Estimating Sea Surface Velocities from Sequential Satellite Images." *Journal of Atmospheric and Oceanic Technology* 7: 852–865. doi:[10.1175/1520-0426\(1990\)007<0852:EOTMCC>2.0.CO;2](https://doi.org/10.1175/1520-0426(1990)007<0852:EOTMCC>2.0.CO;2).
- Yang, H., J. K. Choi, Y.-J. Park, H.-J. Han, and J.-H. Ryu. 2014. "Application of the Geostationary Ocean Color Imager (GOCI) to Estimates of Ocean Surface Currents." *Journal of Geophysical Research* 119 (6): 3988–4000. doi:[10.1002/2014JC009981](https://doi.org/10.1002/2014JC009981).
- Yiğiterhan, O., J. W. Murray, and S. Tuğrul. 2011. "Trace Metal Composition of Suspended Particulate Matter in the Water Column of the Black Sea." *Marine Chemistry* 126 (1): 207–228. doi:[10.1016/j.marchem.2011.05.006](https://doi.org/10.1016/j.marchem.2011.05.006).
- Zavialov, P. O., J. V. Grigorieva, O. O. Miller, A. G. Kostianoy Jr., and M. Gregoire. 2002. "Continuity Preserving Modified Maximum Cross-Correlation Technique." *Journal of Geophysical Research* 107 (C10): 3160. doi:[10.1029/2001JC001116](https://doi.org/10.1029/2001JC001116).